Mon. Not. R. Astron. Soc. **387,** 921–932 (2008) doi:10.1111/j.1365-2966.2008.13304.x

The assembly bias of dark matter haloes to higher orders

R. E. Angulo,★ C. M. Baugh★ and C. G. Lacey★
Institute for Computational Cosmology, Department of Physics, University of Durham, South Road, Durham DH1 3LE

Accepted 2008 April 7. Received 2008 April 7; in original form 2007 December 14

ABSTRACT

We use an extremely large volume ($2.4\,h^{-3}$ Gpc^3), high-resolution N-body simulation to measure the higher order clustering of dark matter haloes as a function of mass and internal structure. As a result of the large simulation volume and the use of a novel 'cross-moment' counts-in-cells technique which suppresses discreteness noise, we are able to measure the clustering of haloes corresponding to rarer peaks than was possible in previous studies; the rarest haloes for which we measure the variance are 100 times more clustered than the dark matter. We are able to extract, for the first time, halo bias parameters from linear up to fourth order. For all orders measured, we find that the bias parameters are a strong function of mass for haloes more massive than the characteristic mass M_*. Currently, no theoretical model is able to reproduce this mass dependence closely. We find that the bias parameters also depend on the internal structure of the halo up to fourth order. For haloes more massive than M_*, we find that the more concentrated haloes are more weakly clustered than the less concentrated ones. We see no dependence of clustering on concentration for haloes with masses $M < M_*$; this is contrary to the trend reported in the literature when segregating haloes by their formation time. Our results are insensitive to whether haloes are labelled by the total mass returned by the friends-of-friends group finder or by the mass of the most massive substructure. This implies that our conclusions are not an artefact of the particular choice of group finding algorithm. Our results will provide important input to theoretical models of galaxy clustering.

Key words: methods: numerical – galaxies: haloes – cosmology: theory – dark matter.

1 INTRODUCTION

The spatial distribution of dark matter haloes is not as simple as was once suspected. In the standard theoretical model for the abundance and distribution of haloes, the clustering strength of haloes is predicted to be a function of mass alone, with more massive haloes displaying stronger clustering (e.g. Kaiser 1984; Cole & Kaiser 1989; Mo & White 1996). However, recent numerical simulations of hierarchical cosmologies, by covering larger volumes with ever improving mass resolution, have been able to reveal subtle dependences of halo clustering on other properties such as formation redshift, the internal structure of the halo and its spin (Gao, Springel & White 2005; Harker et al. 2006; Wechsler et al. 2006; Bett et al. 2007; Espino-Briones, Plionis & Ragone-Figueroa 2007; Jing et al. 2007; Wetzel et al. 2007).

The dependence of halo clustering on a second parameter in addition to mass is generally referred to as assembly bias. However, the nature of the trend in clustering strength recovered depends upon the choice of property used to classify haloes of a given mass. Early simulation work failed to uncover a convincing assembly bias signal, as a result of insufficient volume and mass resolution, which meant that halo clustering could be measured for only a narrow range of mass and with limited statistics (Lemson & Kauffmann 1999; Percival et al. 2003; Sheth & Tormen 2004). The first clear indication of a dependence of halo clustering on a second property was uncovered by Gao et al. (2005). These authors reported that low-mass haloes which form early are more clustered than haloes of the same mass which form later on. No effect was seen for massive haloes. Wechsler et al. (2006) were able to confirm this result but also found that halo clustering depends on the density profile of the halo, as characterized by the concentration parameter (Navarro, Frenk & White 1997). The sense of the dependence of clustering strength on concentration changes with mass. Wechsler et al. found that massive haloes showed a dependence of clustering strength on concentration, with low-concentration haloes being the more strongly clustered (as confirmed by Gao & White 2007, Jing et al. 2007; Wetzel et al. 2007). This trend of clustering strength with concentration is reversed for low-mass haloes. Although formation time and concentration are correlated (e.g. Neto et al. 2007), their impact on the clustering of haloes does not follow trivially from this correlation, suggesting that some other parameter may be more fundamental (as argued by Croton, Gao & White 2007).

Previous studies of assembly bias have exclusively focused on the linear bias parameter, which relates the two-point correlations

★E-mail: raul.angulo@durham.ac.uk (REA); c.m.baugh@durham.ac.uk (CMB); cedric.lacey@durham.ac.uk (CGL)

of haloes and dark matter. Measurements from local surveys have shown that galaxies have significant higher order correlation functions and that the spatial distribution of galaxies and haloes is not fully described by two-point statistics (e.g. Baugh et al. 2004; Croton et al. 2004; Frith, Outram & Shanks 2006; Nichol et al. 2006). With large surveys planned at higher redshifts, there is a clear need for accurate models of the higher order clustering of dark matter haloes, and to establish whether or not the higher order bias parameters depend on other properties in addition to mass.

In this paper, we measure the higher order bias parameters of dark matter haloes using a simulation which covers a volume more than an order of magnitude larger than the run analysed by Gao and collaborators. We use a novel approach to estimate the higher order correlation functions of dark matter haloes. Our method builds upon the cross-correlation technique advocated for two-point correlations by Jing et al. (2007), Gao & White (2007) and Smith, Scoccimarro & Sheth (2007). By considering fluctuations in the density of haloes and dark matter within the same smoothing window, we can suppress discreteness noise in our measurements. This improved clustering estimator, which uses the counts-in-cells method, when coupled with the large volume of our simulation, allows us to recover the bias parameters from linear to fourth order, and to study the dependence of these parameters on the halo concentration.

In Section 2, we give the theoretical background to the counts-in-cells technique we use to estimate higher order clustering and explain how the clustering of haloes relates to the underlying dark matter at different orders. We also introduce the numerical simulations in that section. We present our results in Section 3 and a summary and discussion in Section 4.

2 THEORETICAL BACKGROUND AND METHOD

In this section, we give the theoretical background to the measurements presented in Section 3. We estimate the clustering of haloes and dark matter using a counts-in-cells approach. An overview of this method is given in Section 2.1, in which we explain how to obtain expressions for the higher order autocorrelation functions of a density field from the moments of the distribution of counts-in-cells. We also introduce the concept of higher order *cross*-correlation functions, which combine fluctuations in two density fields. The concept of hierarchical amplitudes, scaling relations between higher order correlation functions and the two-point correlation function is introduced in Section 2.2. The key theoretical results relating the higher order cross-correlation functions of haloes to the two-point function and hierarchical amplitudes of the dark matter are given in Section 2.3. The simulations we use to measure the clustering of dark matter haloes are described in Section 2.4.

2.1 The counts in cells approach to measuring clustering

Here, we give a brief overview of the approach of using the distribution of counts in cells to estimate the higher order autocorrelation functions of a set of objects. An excellent and comprehensive review of this material is given by Bernardeau et al. (2002). We first discuss the higher order correlation functions for the case of a continuous, unsmoothed density field, then introduce the concept of cross-correlations (Section 2.1.1), before explaining how these results are changed in the case of a smoothed distribution of discrete points (Section 2.1.2).

2.1.1 Higher order correlations: unsmoothed and continuous density field

In general, the complete hierarchy of N-point correlation functions is required to fully characterize the spatial distribution of fluctuations in a density field. An exception to this occurs for the special case of a Gaussian density field, which can be described completely by its two-point correlation function.

The N-point correlation functions are usually written in terms of the dimensionless density fluctuation or density contrast at a point:

$$\delta(x) = \rho(x)/\langle\rho\rangle - 1, \tag{1}$$

where $\langle\rho\rangle$ is the mean density, the average is taken over different spatial locations. By definition, $\langle\delta(x)\rangle = 0$ when the average is taken over a fair sample of the density field. The Nth-order moment of the density field, sometimes referred to as a central moment because δ is a fractional fluctuation around the mean density, is given by

$$\mu_N = \langle\delta(x_1), \ldots, \delta(x_n)\rangle, \tag{2}$$

where, in general, the density fluctuations are correlated at different spatial locations.

The Nth-order central moments defined in equation (2) can be decomposed into terms which include products of lower order moments. This is because there are different permutations of how the N-points can be 'connected' or joined together. This idea is illustrated nicely by tree diagrams in the review by Bernardeau et al. (2002). The terms into which the central moments are broken down are called connected moments and these cannot be reduced further. In the tree diagram language, an N-point connected moment has no disjoint points; all N-points are linked to one another when the spatial averaging is performed. The distinction between connected and unconnected moments may become clearer if we write down the decomposition of the unconnected central moments up to fifth order:

$$\langle\delta^2\rangle = \langle\delta^2\rangle_c + \langle\delta\rangle_c^2 \tag{3}$$

$$\langle\delta^3\rangle = \langle\delta^3\rangle_c + 3\langle\delta^2\rangle_c\langle\delta\rangle_c + \langle\delta\rangle_c^3 \tag{4}$$

$$\begin{aligned}\langle\delta^4\rangle = {} & \langle\delta^4\rangle_c + 4\langle\delta^3\rangle_c\langle\delta\rangle_c + 3\langle\delta^2\rangle_c^2 \\ & + 6\langle\delta^2\rangle_c\langle\delta\rangle_c^2 + \langle\delta\rangle_c^4\end{aligned} \tag{5}$$

$$\begin{aligned}\langle\delta^5\rangle = {} & \langle\delta^5\rangle_c + 5\langle\delta^4\rangle_c\langle\delta\rangle_c + 10\langle\delta^3\rangle_c\langle\delta^2\rangle_c \\ & + 10\langle\delta^3\rangle_c\langle\delta\rangle_c^2 + 15\langle\delta^2\rangle_c^2\langle\delta\rangle_c \\ & + 10\langle\delta^2\rangle_c\langle\delta\rangle_c^3 + \langle\delta\rangle_c^5,\end{aligned} \tag{6}$$

where the subscript c outside the angular brackets denotes a connected moment. Remembering that $\langle\delta\rangle = 0$, these equations simplify to

$$\langle\delta^2\rangle = \langle\delta^2\rangle_c \tag{7}$$

$$\langle\delta^3\rangle = \langle\delta^3\rangle_c \tag{8}$$

$$\langle\delta^4\rangle = \langle\delta^4\rangle_c + 3\langle\delta^2\rangle_c^2 \tag{9}$$

$$\langle\delta^5\rangle = \langle\delta^5\rangle_c + 10\langle\delta^3\rangle_c\langle\delta^2\rangle_c. \tag{10}$$

Hence, for the second- and third-order moments, there is no difference in practice between the connected and unconnected moments.

The N-point autocorrelation functions, ξ_N, are written in terms of the connected moments:

$$\xi_N(x_1, \ldots, x_N) = \langle\delta(x_1), \ldots, \delta(x_N)\rangle_c. \tag{11}$$

By analogy with the N-point autocorrelation functions of fluctuations in a single density field, we can define the $i + j$-point cross-correlation function of two, co-spatial density fields, with respective density contrasts given by δ_1 and δ_2:

$$\xi_{i,j}(x_1, \ldots, x_i \quad ; \quad y_1, \ldots y_j) = \langle \delta_1(x_1), \ldots, \delta_1(x_i)\, \delta_2(y_1), \ldots, \delta_2(y_j) \rangle_c. \tag{12}$$

In the application in this paper, the first index will refer to the distribution of dark matter haloes and the second index to the dark matter. When the density contrasts are evaluated at the same spatial location, i.e. $x_1 = \cdots = x_i = y_1 = \cdots = y_j = 0$, the connected moments $\xi_{i,j}$ are called cumulants of the joint probability distribution function of δ_1 and δ_2 (and are sometimes denoted as $k_{i,j}$).

To generate expressions for the higher order correlation functions of the cross-correlated density fluctuations, $\xi_{i,j}$, we will use the method of generating functions (see section 3.3.3 of Bernardeau et al. 2002). A moment generating function is defined for the central moments ($\mu_{i,j}$) as a power series in δ_1 and δ_2, which can be written as $\chi \equiv \langle \exp(\delta_1 t_1 + \delta_2 t_2) \rangle$, where t_1 and t_2 are random variables. This moment generating function can be related to the cumulant generating function (ψ) for the connected cumulants by (see Bernardeau et al. 2002 for a proof)

$$\psi(t_1, t_2) \equiv \ln \chi(t_1, t_2). \tag{13}$$

Then, by taking partial derivatives of ψ and χ evaluated at $t_1 = t_2 = 0$, one can 'generate' the cumulants and moments:

$$\xi_{i,j}(0) = k_{i,j} = \frac{\partial^{i+j}}{\partial t_1^i\, \partial t_2^j} \psi|_{t_1=t_2=0} \tag{14}$$

$$\mu_{i,j} = \frac{\partial^{i+j}}{\partial t_1^i\, \partial t_2^j} \chi|_{t_1=t_2=0} = \left\langle \delta_1^i \delta_2^j \right\rangle. \tag{15}$$

Following this method, we can obtain expressions for the cross-correlation cumulants up to the order of $i + j = 5$, grouping terms of the same order:

$$k_{1,1} = \mu_{1,1} \tag{16}$$

$$k_{2,0} = \mu_{2,0} \tag{17}$$

$$k_{3,0} = \mu_{3,0} \tag{18}$$

$$k_{2,1} = \mu_{2,1} \tag{19}$$

$$k_{4,0} = \mu_{4,0} - 3\, {\mu_{2,0}}^2 \tag{20}$$

$$k_{3,1} = \mu_{3,1} - 3\, \mu_{2,0} \mu_{1,1} \tag{21}$$

$$k_{2,2} = \mu_{2,2} - \mu_{2,0} \mu_{0,2} - 2\, {\mu_{1,1}}^2 \tag{22}$$

$$k_{5,0} = \mu_{5,0} - 10\, \mu_{3,0} \mu_{2,0} \tag{23}$$

$$k_{4,1} = \mu_{4,1} - 4\, \mu_{3,0} \mu_{1,1} - 6\, \mu_{2,0} \mu_{2,1} \tag{24}$$

$$k_{3,2} = \mu_{3,2} - \mu_{3,0} \mu_{0,2} - 6\, \mu_{2,1} \mu_{1,1} - 3\, \mu_{2,0} \mu_{1,2}. \tag{25}$$

Note that these results are symmetric with respect to exchanging the indexes and that we have used the fact that $\mu_{1,0} = \mu_{0,1} = 0$, since, by construction $\langle \delta_1 \rangle = \langle \delta_2 \rangle = 0$.

2.1.2 Higher order correlations: smoothed and discrete density fields

Sadly, density fluctuations at a point are of little practical use as they cannot be measured reliably. Typically we have a finite number of tracers of the density field (i.e. galaxies in a survey or dark matter particles in an N-body simulation) and so we have a limited resolution view of the density field. Furthermore, estimating the N-point correlations for a modern survey or simulation is time consuming and shortcuts are often taken, such as restricting the number of configurations of points sampled. To overcome both of these problems, moments of the smoothed density field can be computed instead of the point moments.

The smoothed density contrast, δ_R, is a convolution of the density contrast at a point with the smoothing window, W_R, which has volume V:

$$\delta(x)_R = \frac{1}{V} \int \mathrm{d}x^{3'} \delta(x) W_R(x - x'). \tag{26}$$

Typically, the smoothing window is a spherical top-hat in which case $W_R = 1$ for all points within distance R from the centre of the window and $W_R = 0$ otherwise. After smoothing, the cumulants correspond to the $i + j$-point volume-averaged cross-correlation functions:

$$\bar{\xi}_{i,j}(R) \equiv \int \mathrm{d}^3 x_1 \ldots \mathrm{d}^3 x_i \quad \mathrm{d}^3 y_1 \ldots \mathrm{d}^3 y_j \times W_R(x_1) \ldots W_R(x_i)\, W_R(y_1) \ldots W_R(y_j) \xi_{i,j}. \tag{27}$$

Equations (16)–(25) are still valid, with the cumulants replaced by volume-averaged cumulants.

Another issue introduced by the discreteness of the density field is the contribution of Poisson noise to the measurements of the cumulants. To take this into account, we can modify the moment generating function as follows (Peebles 1980):

$$\chi(t_1, t_2) = \langle \exp(f_1(t_1) + f_2(t_2)) \rangle, \tag{28}$$

$$f_1 = (\exp(t_1) - t_1 - 1)\, \bar{n}_1 + (\exp(t_1) - 1)\, \delta_1, \tag{29}$$

$$f_2 = (\exp(t_2) - t_2 - 1)\, \bar{n}_2 + (\exp(t_2) - 1)\, \delta_2. \tag{30}$$

Here, $\bar{n}_1$ and $\bar{n}_2$ are the mean number of objects in density field 1 and density field 2, respectively, within spheres of radius R. Using this modified generating function, and defining $\mu'_{i,j} = \langle (n_1 - \bar{n}_1)^i (n_2 - \bar{n}_2)^j \rangle$, we obtain the following relations between the volume-averaged, connected $i + j$-point cross-correlation functions, $\bar{\xi}_{i,j}$, and the central moments, $\mu_{i,j}$:

$$\bar{n}_1^2\, \bar{\xi}_{2,0} = \mu'_{2,0} - \bar{n}_1 \tag{31}$$

$$\bar{n}_1 \bar{n}_2\, \bar{\xi}_{1,1} = \mu'_{1,1} \tag{32}$$

$$\bar{n}_2^2\, \bar{\xi}_{0,2} = \mu'_{0,2} - \bar{n}_2 \tag{33}$$

$$\bar{n}_1^3\, \bar{\xi}_{3,0} = \mu'_{3,0} + 2\bar{n}_1 - 3\mu'_{2,0} \tag{34}$$

$$\bar{n}_1^2 \bar{n}_2\, \bar{\xi}_{2,1} = \mu'_{2,1} - \mu'_{1,1} \tag{35}$$

$$\bar{n}_1 \bar{n}_2^2\, \bar{\xi}_{1,2} = \mu'_{1,2} - \mu'_{1,1} \tag{36}$$

$$\bar{n}_2^3\, \bar{\xi}_{0,3} = \mu'_{0,3} + 2\bar{n}_2 - 3\mu'_{0,2} \tag{37}$$

$$\bar{n}_1^4\, \bar{\xi}_{4,0} = \mu'_{4,0} - 6\bar{n}_1 + 11\mu'_{2,0} - 6\mu'_{3,0} - 3\mu'^2_{2,0} \tag{38}$$

$$\bar{n}_1^3 \bar{n}_2 \, \bar{\xi}_{3,1} = \mu'_{3,1} + 2\mu'_{1,1} - 3\mu'_{2,1} - 3\mu'_{1,1}\mu'_{2,0} \quad (39)$$

$$\bar{n}_1^2 \bar{n}_2^2 \, \bar{\xi}_{2,2} = \mu'_{2,2} - \mu'_{1,2} - \mu'_{2,1} + \mu'_{1,1} - \mu'_{2,0}\mu'_{0,2} - 2\mu'^2_{1,1} \quad (40)$$

$$\bar{n}_1 \bar{n}_2^3 \, \bar{\xi}_{1,3} = \mu'_{1,3} + 2\mu'_{1,1} - 3\mu'_{1,2} - 3\mu'_{1,1}\mu'_{0,2} \quad (41)$$

$$\bar{n}_2^4 \, \bar{\xi}_{0,4} = \mu'_{0,4} - 6n_2 + 11\mu'_{0,2} - 6\mu'_{0,3} - 3\mu'^2_{0,2}. \quad (42)$$

Note that these expressions revert to those in the literature for autocorrelation moments in the case of either i or j equal to zero (see e.g. Baugh, Gaztanaga & Efstathiou 1995). Also note that in the limit $\bar{n}_1 \to \infty$, $\bar{n}_2 \to \infty$, they correspond to the expressions given by equations (16)–(25).

2.2 Hierarchical amplitudes

At this point, it is useful to define quantities called hierarchical amplitudes which are the ratio between the N-point, volume-averaged connected moments and the two-point volume-averaged connected moment raised to the $N-1$ power:

$$S_N \equiv \frac{\bar{\xi}_N}{\bar{\xi}_2^{N-1}}. \quad (43)$$

This form is motivated by the expected properties of a Gaussian field which evolves due to gravitational instability (Bernardeau et al. 2002). In the case of small amplitude fluctuations, i.e. on smoothing scales for which $\bar{\xi}_2(R) \ll 1$, the S_N depend only on the local slope of the linear perturbation theory power spectrum of density fluctuations and are independent of time (Juszkiewicz, Bouchet & Colombi 1993; see Bernardeau 1994 for expressions for the S_N). Similar scalings, but with different values for the S_N, apply in the case of distributions of particles which have not arisen through gravitational instability, e.g. particles displaced according to the Zel'dovich approximation (see Juszkiewicz et al. 1993).

In the case of a Gaussian density field, all of the S_N are equal to zero. Initially, as perturbations grow through gravitational instability, the two-point connected moment increases. The distribution of fluctuations soon starts to deviate from a Gaussian, particularly as voids grow in size and cells become empty ($\delta \to -1$). Voids evolve more slowly than overdense regions. There is in principle no limit on how overdense a cell can become. As a result, the distribution of overdensities becomes asymmetrical or skewed, with the peak of the distribution moving to negative density contrasts and a long tail developing to high-density contrasts. To first order, this deviation from symmetry is quantified by the value of S_3, which is often referred to as the skewness of the density field. Higher order moments and hierarchical amplitudes probe progressively further out into the tails of the distribution of density contrasts.

2.3 Higher order correlations: biased tracers

We are now in a position to consider the cross-correlation functions for the case of relevance in this paper, when the set of objects making up one of the density fields is local function of the second density field; the first density field is a biased tracer of the second. In our application, one density field is defined by the spatial distribution of dark matter haloes and the other by the dark matter. In the case of a local bias and small perturbations, the density contrast in the biased tracers (δ_1) can be written as an expansion in terms of the underlying dark matter density contrast (δ_2), as proposed by Fry & Gaztanaga (1993)

$$\delta_1(R) = \sum_{k=0}^{\infty} \frac{b_k}{k!} \delta_2^k(R), \quad (44)$$

where the b_k are known as bias coefficients and b_1 is the linear bias commonly discussed in relation to two-point correlations. Note that, by construction, we require that $\langle \delta \rangle = 0$, which implies $b_0 = -\sum_{k=2}^{\infty} \langle b_k \rangle / k!$. The b_k, as we will see later, depends on mass but this is suppressed in our notation.

Using this bias prescription, and following the treatment Fry & Gaztanaga (1993) used for autocorrelations, we can write the volume-averaged cross-correlation functions of dark matter haloes in terms of the two-point volume-averaged correlation function ($\bar{\xi}_{0,2}$) and hierarchical amplitudes of the dark matter, S_N:

$$\bar{\xi}_{1,1} = b_1 \bar{\xi}_{0,2} + O\left(\bar{\xi}_{0,2}^2\right) \quad (45)$$

$$\bar{\xi}_{2,0} = b_1^2 \bar{\xi}_{0,2} + O\left(\bar{\xi}_{0,2}^2\right) \quad (46)$$

$$\bar{\xi}_{1,2} = b_1 \bar{\xi}_{0,2}^2 \, (c_2 + S_3) + O\left(\bar{\xi}_{0,2}^3\right) \quad (47)$$

$$\bar{\xi}_{2,1} = b_1^2 \bar{\xi}_{0,2}^2 \, (2\,c_2 + S_3) + O\left(\bar{\xi}_{0,2}^3\right) \quad (48)$$

$$\bar{\xi}_{3,0} = b_1^3 \bar{\xi}_{0,2}^2 \, (3\,c_2 + S_3) + O\left(\bar{\xi}_{0,2}^3\right) \quad (49)$$

$$\bar{\xi}_{1,3} = b_1 \bar{\xi}_{0,2}^3 \, (3S_3 c_2 + S_4 + c_3) + O\left(\bar{\xi}_{0,2}^4\right) \quad (50)$$

$$\bar{\xi}_{2,2} = b_1^2 \bar{\xi}_{0,2}^3 \left(S_4 + 6S_3 c_2 + 2c_2^2 + 2c_3\right) + O\left(\bar{\xi}_{0,2}^4\right) \quad (51)$$

$$\bar{\xi}_{3,1} = b_1^3 \bar{\xi}_{0,2}^3 \left(6c_2^2 + 9S_3 c_2 + S_4 + 3c_3\right) + O\left(\bar{\xi}_{0,2}^4\right) \quad (52)$$

$$\bar{\xi}_{4,0} = b_1^4 \bar{\xi}_{0,2}^3 \left(12c_2^2 + 12S_3 c_2 + S_4 + 4c_3\right) + O\left(\bar{\xi}_{0,2}^4\right) \quad (53)$$

$$\bar{\xi}_{1,4} = b_1 \bar{\xi}_{0,2}^4 \left(4c_2 S_4 + 6c_3 S_3 + c_4 + S_5 + 3c_2 S_3^2\right) + O\left(\bar{\xi}_{0,2}^5\right) \quad (54)$$

$$\bar{\xi}_{2,3} = b_1^2 \bar{\xi}_{0,2}^4 \left(12S_3 c_3 + 6S_3^2 c_2 + 12S_3 c_2^2 + 6c_2 c_3 + 2c_4 + S_5 + 8c_2 S_4\right) + O\left(\bar{\xi}_2^5\right) \quad (55)$$

$$\bar{\xi}_{3,2} = b_1^3 \bar{\xi}_{0,2}^4 \left(12c_2 S_4 + 18c_3 S_3 + 18c_2 c_3 + 36c_2^2 S_3 + 9c_2 S_3^2 + S_5 + 6c_2^3 + 3c_4\right) + O\left(\bar{\xi}_2^5\right) \quad (56)$$

$$\bar{\xi}_{4,1} = b_1^4 \bar{\xi}_{0,2}^4 \left(4c_4 + 24c_2^3 + S_5 + 72c_2^2 S_3 + 16c_2 S_4 + 36c_2 c_3 + 24c_3 S_3 + 12c_2 S_3^2\right) + O\left(\bar{\xi}_2^5\right) \quad (57)$$

$$\bar{\xi}_{5,0} = b_1^5 \bar{\xi}_{0,2}^4 \left(20c_2 S_4 + 15c_2 S_3^2 + 60c_2^3 + 30c_3 S_3 + 5c_4 + 120c_2^2 S_3 + S_5 + 60c_2 c_3\right) + O\left(\bar{\xi}_2^5\right) \quad (58)$$

where $c_k = b_k / b_1$. Note that it has been shown that these transformations preserve the hierarchical nature of the clustering (Fry & Gaztanaga 1993).

2.4 Numerical Simulations

To make accurate measurements of the higher order clustering of dark matter and dark matter haloes, we use the *N*-body simulations carried out by Angulo et al. (2008). Two simulation specifications were used: (i) The BASICC, a high-resolution run which used 1448^3 particles of mass $5.49 \times 10^{11}\, h^{-1}\, \mathrm{M}_\odot$ to follow the growth of structure in the dark matter in a periodic box of side $1340\, h^{-1}$ Mpc. (ii) The L-BASICC ensemble, a suite of 50 lower resolution runs, which used 448^3 particles of mass $1.85 \times 10^{12}\, h^{-1}\, \mathrm{M}_\odot$ in the same box size as the BASICC. Each L-BASICC run was evolved from a different realization of the initial Gaussian density field. The simulation volume was chosen to allow the growth of fluctuations to be modelled accurately on a wide range of scales, including that of the baryonic acoustic oscillations (the acronym BASICC stands for Baryonic Acoustic oscillation Simulations at the Institute for Computational Cosmology). The extremely large volume of each box also makes it possible to extract accurate measurements of the clustering of massive haloes. The superior mass resolution of the BASICC run means that it can resolve the haloes which are predicted to host the galaxies expected to be seen in forthcoming galaxy surveys. The L-BASICC runs resolve haloes equivalent to group-sized systems. The independence of the L-BASICC ensemble runs makes them ideally suited to the assessment of the impact of cosmic variance on our clustering measurements.

In both cases, the same values of the basic cosmological parameters were adopted, which are broadly consistent with recent data from the cosmic microwave background and the power spectrum of galaxy clustering (Sánchez et al. 2006): the matter density parameter, $\Omega_\mathrm{M} = 0.25$, the vacuum energy density parameter, $\Omega_\Lambda = 0.75$, the normalization of density fluctuations, expressed in terms of the linear theory amplitude of density fluctuations in spheres of radius $8\, h^{-1}$Mpc at the present day, $\sigma_8 = 0.9$, the primordial spectral index $n_\mathrm{s} = 1$, the dark energy equation of state, $w = -1$, and the Hubble constant, $h = H_0/(100\,\mathrm{km\,s^{-1}\,Mpc^{-1}}) = 0.73$. The simulations were started from realizations of a Gaussian density field set up using the Zel'dovich approximation (Zel'Dovich 1970). Particles were perturbed from a glass-like distribution (White 1994; Baugh et al. 1995). The starting redshift for both sets of simulations was $z = 63$. The linear perturbation theory power spectrum used to set up the initial density field was generated using the Boltzman code CAMB (Lewis, Challinor & Lasenby 2000). The initial density field was evolved to the present day using a memory efficient version of GADGET-2 (Springel 2005).

Outputs of the particle positions and velocities were stored from the simulations at selected redshifts. Dark matter haloes were identified using the Friends-of-Friends (FOF) percolation algorithm (Davis et al. 1985) and substructures within these were found using a modified version of SUBFIND (Springel et al. 2001). Our default choice is to use the number of particles in a structure as returned by the FOF group finder to set the mass of the halo; at the end of Section 3.4 we discuss a variation on this to assess the sensitivity of our results to the group finder. The position of the halo is the position of the most bound particle in the largest substructure, as determined by SUBFIND. In this paper, only gravitationally bound groups with more than 26 particles are considered. The SUBFIND algorithm also computes several halo properties such as the circular velocity profile $V_\mathrm{c}(r) = (GM(r)/r)^{1/2}$, V_max, the maximum value of V_c for the largest substructure, and $V_{200} = V_\mathrm{c}(r_{200})$, where r_{200} is the radius of a sphere enclosing a volume of mean density 200 times the critical density. These properties are calculated using only the particles which are bound to the main subhalo of the FOF halo; i.e. ignoring all of the other substructure haloes within the FOF halo. In the best resolved haloes, substructures other than the largest substructure account for at the most 15 per cent of the total halo mass (Ghigna et al. 1998). Later on in the paper, we will present results for the clustering of haloes as a function of mass and a second parameter. We have a limited number of output times available to us, so it is not feasible to use the formation time of the halo as the second parameter. Instead, we will use the ratio V_max/V_{200}. Fig. 1 shows V_max/V_{200} as a function of halo mass at different epochs in the BASICC simulation. There is a trend of declining V_max/V_{200} with increasing halo mass. In cases where the density profile of the dark matter halo matches the universal profile advocated by Navarro et al. (1997), V_max/V_{200} depends on the concentration parameter which characterizes the profile. Haloes in the extreme parts of the distribution of V_max/V_{200} also have extreme values of the concentration parameter (Navarro et al. 1997). More massive haloes tend to have lower values of the concentration parameter and lower values of the velocity ratio V_max/V_{200}. The ratio V_max/V_{200} is easier to extract from the simulation, as it does not require a parametric form to be fitted to the density profile. There is a correlation between formation time and concentration parameter, and hence the ratio V_max/V_{200}, albeit with scatter (Navarro et al. 1997; Zhao et al. 2003).

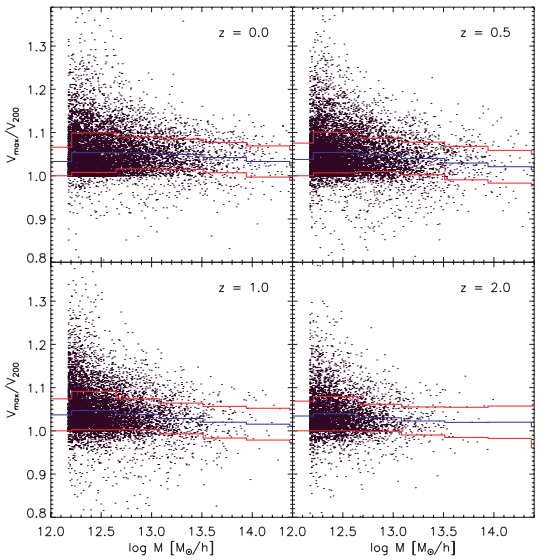

Figure 1. The ratio V_max/V_{200} as a function of halo mass for gravitationally bound haloes in the BASICC simulation, which have a minimum of 26 particles. V_max is the maximum effective circular velocity of the largest substructure within the halo and V_{200} is the effective rotation speed at the radius within which the mean density is 200 times the critical density, computed using all of the particles within this radius. Each panel shows the relation at a different redshift as indicated by the legend. The red lines show the 20–80 percentile range of the distribution of V_max/V_{200} values, and the blue lines show the mean.

3 RESULTS

Our ultimate goal is to measure the higher order bias of dark matter haloes. As described in Section 2, we follow a novel approach to do this, employing cross moments between haloes and the dark matter. The first step in this process is to compute the densities of haloes and dark matter on grids of cubical cells of different

sizes.[1] A natural by-product of this procedure is the higher order clustering of the dark matter and haloes in terms of the autocorrelation functions. We first present the hierarchical amplitudes estimated for the dark matter (Section 3.1) and haloes (Section 3.2) using the autocorrelation function higher order moments. In Section 3.3, we show the measurements of the cross moments and in Section 3.4 we present the interpretation of these results in terms of the bias parameters.

3.1 Hierarchical amplitudes for the dark matter

Fig. 2 shows the hierarchical amplitudes S_N measured for the dark matter at different redshifts. The upper panels show the results in real space and the lower panels include the effects of redshift space distortions using the distant observer approximation. The points indicate the median value of the hierarchical amplitudes measured in the L-BASICC ensemble and the error bars indicate the variance in these measurements. The lines show the hierarchical amplitudes predicted by perturbation theory (Juszkiewicz et al. 1993; Bernardeau 1994). At the highest redshift plotted, $z = 4$, the agreement between the measurements made from the simulations and the predictions of perturbation theory is impressive, covering scales from 5 to $100\,h^{-1}$ Mpc for S_3 and S_4. As redshift decreases, the simulation results for S_5 and S_6 are slightly higher than the perturbation theory predictions. The measurements of S_3 from the simulations continue to agree with the perturbation theory predictions, but over a narrower range of scales. For smoothing scales on which the variance is less than unity, the hierarchical amplitudes are expected to be independent of epoch, depending only on the shape of the linear perturbation theory power spectrum of density fluctuations (Juszkiewicz et al. 1993; Bernardeau 1994; Gaztanaga & Baugh 1995). Fig. 2 confirms that this is the case. As the density field evolves, the measured hierarchical amplitudes change remarkably little, particularly when one bears in mind that the higher order correlation functions change substantially between $z = 4$ and 0. For example, for a cell of radius $50\,h^{-1}$ Mpc, the two-point volume-averaged correlation function increases by a factor of 14 over this redshift interval, and the three-point function by a factor of 197.

Nevertheless, the simulation results do tend to exceed the perturbation theory predictions on all scales at all orders as the density fluctuations grow.

The hierarchical amplitudes measured on small scales differ significantly from the predictions of perturbation theory. At $z = 4$, the simulation results are below the analytical predictions for cell radii smaller than $R \sim 5\,h^{-1}$ Mpc. This behaviour is sensitive to the arrangement of particles, which is perturbed to set up the initial density field. At later times, the memory of the initial conditions is erased on small scales and the measured amplitudes greatly exceed the expectations of perturbation theory. On these scales, the dominant contribution to the cross-correlation moments is from particles within common dark matter haloes. Note that in Fig. 2 we do not correct the measured higher order correlation functions for Poisson noise, since the initial density field was created by perturbing particles distributed in a glass-like configuration which is sub-Poissonian. Hence, the dark matter density field is not a random sampling of a continuous density field (see Angulo et al. 2008 for an extended discussion of this point). The turnover in the hierarchical amplitudes seen at small cell radii (e.g. for $R < 2\,h^{-1}$ Mpc) is due to the finite resolution of the L-BASICC simulations; the hierarchical amplitudes continue to increase in amplitude on smaller smoothing scales in the BASICC run.

The lower panels of Fig. 2 show the impact of gravitationally induced peculiar motions on the hierarchical amplitudes. We model redshift space distortions using the distant observer approximation, in which peculiar motions perturb the particle position parallel to one of the co-ordinate axes. Virialized structures appear elongated when viewed in redshift space. On large scales, coherent bulk flows tend to increase the amplitude of correlation functions. There is a modest reduction in the amplitude of the hierarchical amplitudes on large scales. On small scales, there is a dramatic reduction in the magnitude of the S_N. The overall impact of the redshift space distortions is to greatly reduce the dependence of the hierarchical amplitudes on smoothing scale (see Hoyle, Szapudi & Baugh 2000).

The estimated error on the measured hierarchical moments is shown in Fig. 3, in which we plot the fractional error on S_N obtained from the scatter in the measurements from the L-BASICC ensemble. The plot suggests that the skewness of the dark matter can be well measured on all smoothing scales considered from a volume of the size of the L-BASICC simulation cube. The range of scales over which robust measurements can be made of the hierarchical amplitudes becomes progressively narrower with increasing order. For example, at $z = 0$, reliable measurements of S_6 are limited to smoothing radii smaller than $R \sim 30\,h^{-1}$ Mpc.

3.2 The hierarchical amplitudes of dark matter haloes

The hierarchical amplitudes of dark matter haloes are more complicated than those of the dark matter. In addition to a term arising from the evolution of the density field under gravitational instability, there is a contribution which depends upon the height of the peak in the initial density field which collapses to form the halo (Mo, Jing & White 1997). For example, if we consider the second- and third-order autocorrelation functions of haloes given by equations (44) and (47), then the skewness for dark matter haloes, $S_3^{\rm H}$, is given by

$$S_3^{\rm H} = \frac{\bar{\xi}_{3,0}}{\left(\bar{\xi}_{2,0}\right)^2} \tag{59}$$

$$= \frac{3b_2}{b_1^2} + \frac{S_3}{b_1}. \tag{60}$$

The gravitational contribution to the skewness, S_3, is diluted by the linear bias factor, b_1. In the case of rare peaks, or, equivalently, haloes with masses far in excess of the characteristic mass, M_*, at a given redshift, $S_3^{\rm H}$ approaches an asymptotic value. In this limit, $b_{\rm k} \approx b_1^k$ and so $S_3^{\rm H} \approx 3$; similar arguments for the fourth- and fifth-order hierarchical amplitudes yield asymptotic values of $S_4^{\rm H} = 16$ and $S_5^{\rm H} = 125$ (Mo et al. 1997). Massive haloes at high redshift can therefore have non-zero hierarchical amplitudes even if the dark matter distribution still has a Gaussian distribution and hence $S_{\rm p}^{\rm DM} = 0$.

We plot the hierarchical amplitudes of dark matter haloes in Fig. 4, as a function of the scaled peak height, $\delta_{\rm c}/\sigma(M, z)$. The simulation results are averaged over smoothing radii of $20 < R < 50\,h^{-1}$ Mpc. The dashed line shows the prediction obtained assuming the mass function of Press & Schechter (1974) and the spherical

[1] Tests show that density fluctuations in cubical cells can be readily translated into counts in spherical cells by simply setting the volume of the spherical cell equal to that of the cube. We use cubical cells for speed. The counts are regridded to improve the measurement of the rare event tails of the count distribution.

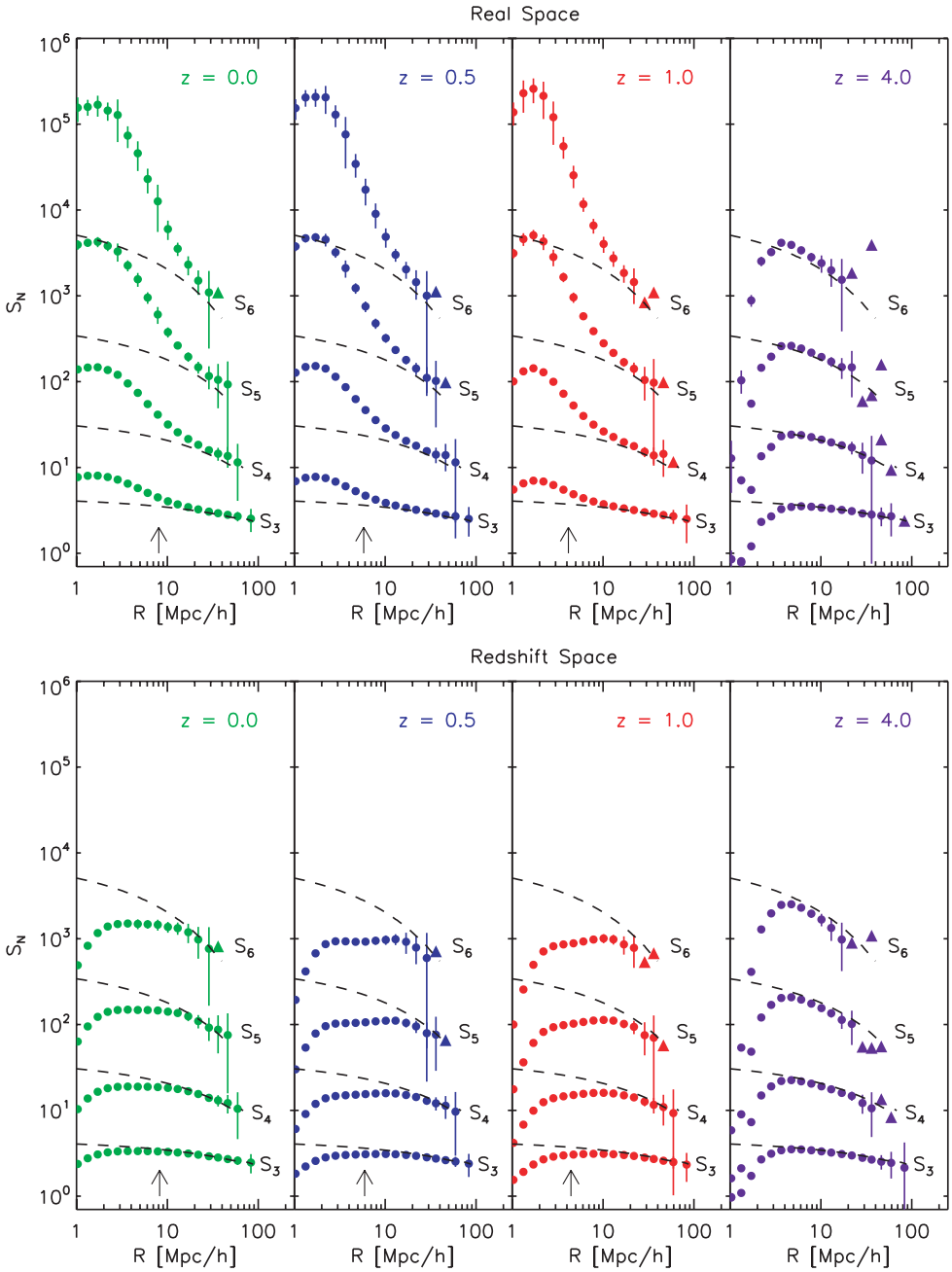

Figure 2. The hierarchical amplitudes (S_N) measured for the dark matter as a function smoothing scale, which is plotted in terms of the radius of the sphere with the same volume as the cubical cell used. The upper panels show the results in real space and the lower panels show redshift space. Each panel corresponds to a different redshift as indicated by the legend. The points show the amplitude for the S_N obtained from the L-BASICC ensemble, after taking the ratio of the median correlation functions, as defined by equation (43). The error bars show the scatter in the measurements over the ensemble, obtained by computing S_N for each simulation from the ensemble. Error bars are plotted at smoothing scales for which the fractional error is less than unity; triangles show scales on which the error exceeds unity. In both sets of panels, the dashed lines show the predictions of perturbation theory in real space (see text for details). Note that no correction for shot noise has been applied to the measured amplitudes. The arrows indicate the cell radius for which the variance in the counts in cells for the dark matter is equal to unity, which is roughly the scale down to which perturbation theory should be valid; at $z = 4$, this scale is below $R = 1\,h^{-1}$ Mpc.

collapse model (see Mo et al. 1997). The solid line shows an improved calculation which uses the ellipsoidal collapse model and the mass function derived by Sheth, Mo & Tormen (2001). There is some dispersion between the simulation results at different redshifts. The measurements are in reasonable agreement with the theoretical predictions for large values of $\delta_c/\sigma(M, z)$. For more modest peaks, the hierarchical amplitudes of haloes averaged on large smoothing scales show a dip and are significantly smaller than the amplitude recovered for the dark matter. The strength of this dip is more pronounced in the measurements from the simulations than it is in the theoretical predictions. This discrepancy suggests that the theoretical models do not reproduce the trend of bias with halo mass for such objects, as we will see in Section 3.4.

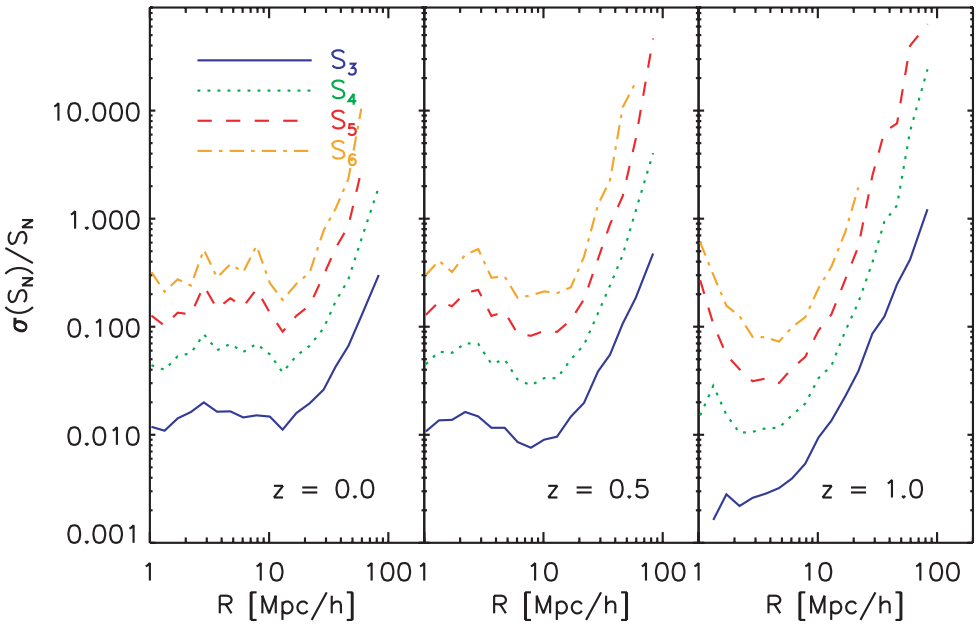

Figure 3. The fractional scatter, $\sigma(S_N)/S_N$, in the measured hierarchical amplitudes, as estimated from the 50 simulations in the L-BASICC ensemble. Different lines show the scatter for different orders as indicated by the legend.

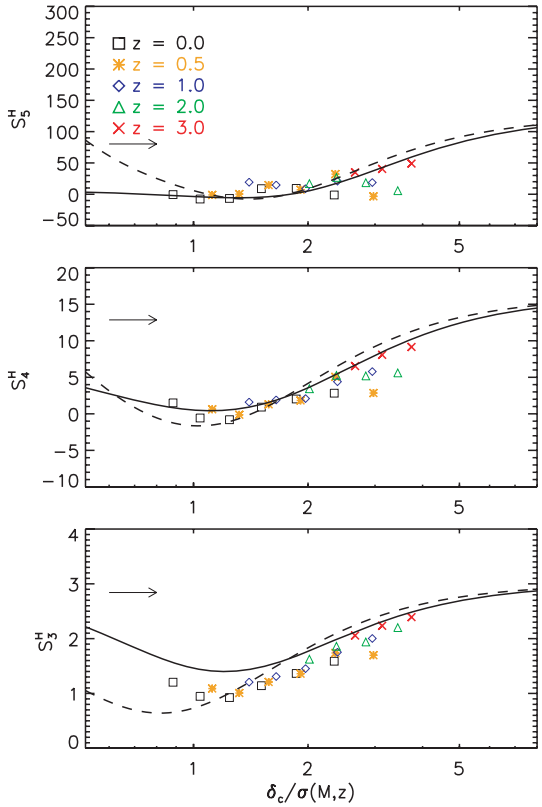

Figure 4. The hierarchical amplitudes of dark matter haloes, plotted as a function of the peak height corresponding to the halo mass. In this plot, the hierarchical amplitudes are averaged over cell sizes of $20 < R < 50\,h^{-1}$ Mpc. The dashed curve shows a theoretical prediction based on the spherical collapse model (Mo et al. 1997) and the solid line shows a revised prediction based upon an ellipsoidal collapse, by Sheth et al. (2001). The corresponding hierarchical amplitudes for the dark matter, averaged over the same range of cell radii, are indicated in each panel by the arrow.

3.3 Cross-correlation estimates of higher order clustering

We now switch to estimating cross-correlation functions instead of autocorrelation functions. To recap Section 2 to reduce the impact of discreteness noise on our measurement of halo clustering, we cross-correlate fluctuations in the spatial distribution of haloes with the fluctuation in the dark matter density within the same cell. As the order of the correlation function increases, the number of possible permutations of halo fluctuations and dark matter fluctuations increases. For a given order of correlation function, the relation between these permutations can be understood using the expressions for the cross-moments given in Section 2.3. The relationship at second order is particularly straightforward. The halo autocorrelation function, $\bar{\xi}_{2,0}$ (recall the first index gives the order of the halo density contrast and the second index gives the order of the dark matter density contrast) is related to the autocorrelation of the dark matter, $\bar{\xi}_{0,2}$, by $\bar{\xi}_{2,0} = b_1^2\bar{\xi}_{0,2}$. The second-order cross-correlation function, $\bar{\xi}_{1,1}$, is related to the autocorrelation function of dark matter by $\bar{\xi}_{1,1} = b_1\bar{\xi}_{0,2}$. The primary difference between $\bar{\xi}_{2,0}$ and $\bar{\xi}_{1,1}$ is therefore a factor of b_1. This basic trend is approximately replicated for any order of correlation function: as fluctuations in the halo density are substituted by fluctuations in the dark matter, the amplitude of the cross-correlation is reduced by a factor which depends on b_1. Above second order, this factor is modulated by higher order bias terms and the hierarchical amplitudes of the dark matter (see Section 2.2). The precise relation between the different permutations of cross-correlation functions depends upon the values of the bias parameters and therefore on the halo mass under consideration.

We show illustrative examples of volume-averaged cross-correlation functions, $\bar{\xi}_{i,j}$, estimated from the BASICC simulation in Fig. 5. Each panel shows a different order of clustering, starting with the second moment in the top left panel and ending with the fifth-order correlation function in the bottom right panel. In this plot, the haloes used have masses in the range $1.1 \times 10^{13} < (M_{\rm halo}/h^{-1}\,{\rm M}_\odot) < 2.8 \times 10^{13}$ and the clustering is measured at $z = 0$. The top-left panel of Fig. 5 shows that there is little difference in the amplitude

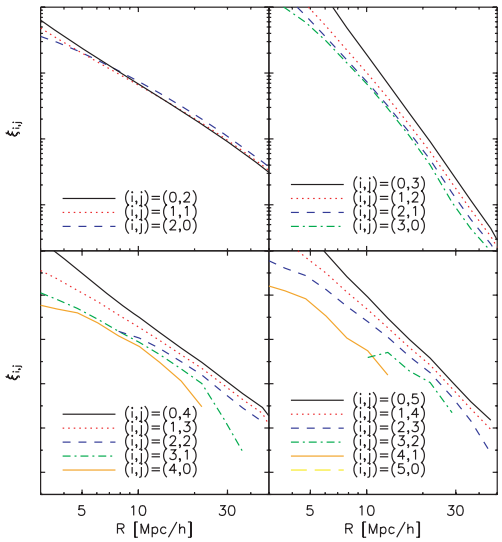

Figure 5. Volume-averaged $i + j$-point cross-correlation functions, $\bar{\xi}_{i,j}$, measured for haloes of mass $1.1 \times 10^{13} < (M/h^{-1}\,\mathrm{M}_{\odot}) < 2.8 \times 10^{13}$ (619 386 objects) and the dark matter at $z = 0$ in the BASICC simulation. The autocorrelation function of haloes is denoted by $\bar{\xi}_{i+j,0}$ and the autocorrelation of dark matter by $\bar{\xi}_{0,i+j}$. Each panel shows a different order of cross-correlation. The key shows the different permutations of cross-correlation function in each case. The moments have been corrected for Poisson noise due to the finite number of haloes.

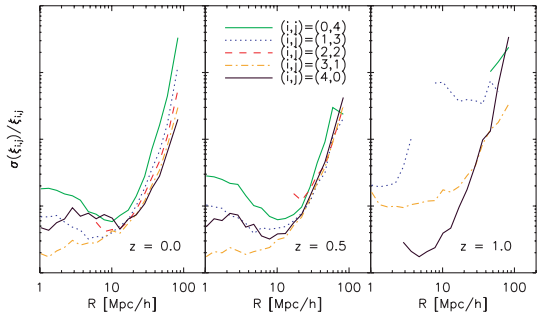

Figure 6. The fractional error on the four-point cross-correlation functions, estimated from the scatter over the L-BASICC runs. Each panel shows the results for a different redshift, as shown by the key. The legend shows the different permutations of cross-correlation moment. To improve the statistics, all the haloes in the L-BASICC runs have been used in this case.

of the second-order correlation function on large smoothing scales between the different permutations of i, j. This implies that for these haloes, the linear bias term $b_1 \approx 1$. The correlation functions are, however, different on small scales. The autocorrelation function of the dark matter ($\bar{\xi}_{0,2}$) is steeper than the autocorrelation of haloes ($\bar{\xi}_{0,2}$). The cross-correlation functions are different on large scales for third, fourth and fifth orders. The difference in amplitude is fairly independent of scale for cells with radii $R > 10\,h^{-1}$ Mpc. Since the linear bias of this sample of haloes is close to unity, this difference is driven by the higher order bias terms and the hierarchical amplitudes of the dark matter. We plan to model the full behaviour of the cross-correlation functions, including the small-scale form, using the halo model in a future paper.

One might be concerned that replacing fluctuations in halo density by fluctuations in dark matter in the higher order correlation functions leads to a reduction in the clustering amplitude (as is indeed apparent in Fig. 5). However, this is more than offset by a reduction in the noise or scatter of the measurement. The fractional error on the measurements of the cross-correlation functions is plotted in Fig. 6. The scatter is estimated using the L-BASICC ensemble. Each panel shows the scatter at a different redshift. The cross-correlation $\bar{\xi}_{1,i+j-1}$ (i.e. one part halo fluctuation, $i + j - 1$ parts dark matter fluctuation) gives the optimal error estimate, with a performance comparable to the autocorrelation of the dark matter. At $z = 1$, it is not possible to measure the four-point autocorrelation function of this sample of haloes, even with a box of the size of the L-BASICC runs. Nevertheless, it is possible to measure the bias factors relating the four-point functions of haloes and mass using the cross-correlation. Our use of a cross-correlation estimator therefore allows us to extend the measurements of the higher order clustering of haloes to orders and redshifts that would not be possible using autocorrelations.

3.4 The bias parameters of dark matter haloes

We now use the cross-correlation functions to estimate the linear and higher order bias parameters of dark matter haloes. As we demonstrated in the previous section, the best possible measurement of the $i + j$th-order correlation function is obtained when the cross-correlation function is made up of one part fluctuation in halo density and $i + j - 1$ parts dark matter fluctuation: i.e. in our notation $\bar{\xi}_{1,i+j-1}$. This approach, combined with the huge volume of our simulation, makes it possible, for the first time, to measure the third- and fourth-order bias parameters, and to do so using narrow mass bins.

In this section, we use the higher resolution BASICC run, which can resolve the largest dynamic range in halo mass. We use the higher order correlation function measurements over the range of smoothing radii $15 < (R/h^{-1}\,\mathrm{Mpc}) < 50$ to estimate the halo bias parameters. The large volume of the BASICC simulation means that we can make robust measurements of the higher order correlation functions out to larger smoothing radii than is possible with the smaller Millennium simulation. The smallest scale we use is set by the requirement that the expansion relating the overdensity in haloes to the overdensity in dark matter (equation 44) is a good approximation, i.e. when $\bar{\xi} \ll 1$. The scales we use to extract the halo bias parameters are considerably larger than those Gao et al. (2005) and Gao & White (2007) were able to use in the Millennium. We use the simulation outputs at redshifts of $z = 0$, 0.5, 1, 2 and 3 to measure the clustering of haloes.

The results for the first-, second-, third- and fourth-order bias parameters of dark matter haloes are presented in Fig. 7. Each panel corresponds to a different order. The upper half of each panel shows the respective order of bias parameter as a function of halo mass, expressed in terms of the peak height corresponding to the halo mass, $\delta_c/\sigma(M, z)$. The lower half of each panel shows the deviation from the bias parameter extracted for a given mass for samples of the 20 per cent of haloes in the mass bin with the highest and lowest values of $V_{\rm max}/V_{200}$, which we are using as a proxy for halo concentration. Different symbols in the upper panels show the measurements at different output redshifts in the BASICC run, as indicated by the key; the same colours are used to draw the lines showing results for samples defined by different $V_{\rm max}/V_{200}$ values at the same output redshifts in the lower panels.

In Fig. 7, there is remarkably little scatter between the results obtained from the different output redshifts for the case of the overall bias as a function of mass. This is encouraging, as it shows that our results are not affected by resolution [haloes with similar values of

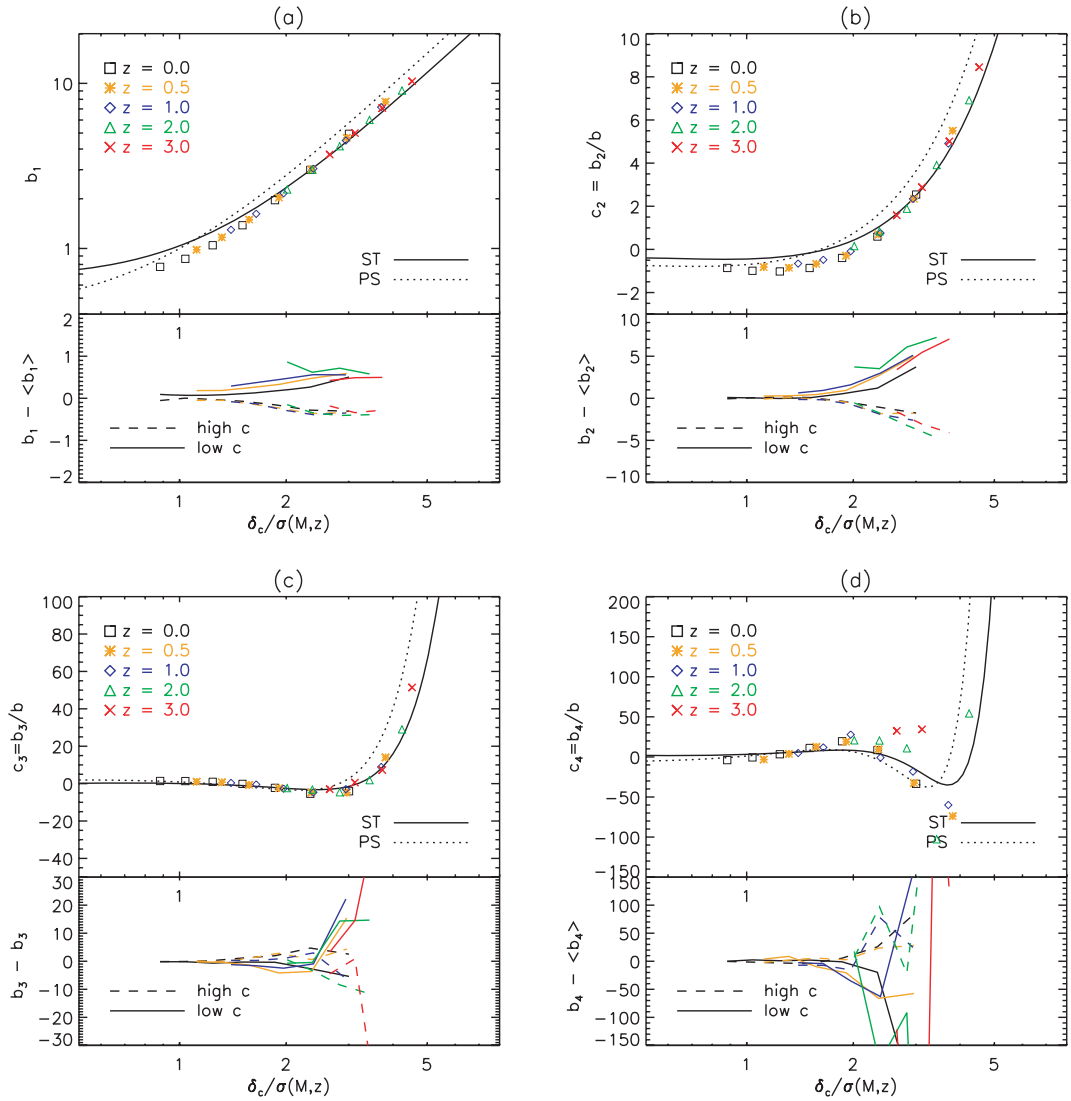

Figure 7. The bias parameters as a function of halo mass parametrized by $\nu = \delta_c/\sigma(M, z)$. Each plot shows a different order of bias parameter: (a) linear bias b_1, (b) the ratio of the second-order bias, b_2/b_1, (c) the ratio of the third-order bias, b_3/b_1 and (d) b_4/b_1. In the lower panel of each plot, the residual bias parameters for the 20 per cent of haloes with the highest or lowest values of V_{max}/V_{200}, a proxy for concentration, are plotted. In the upper panels, symbols show the measurements for different output redshifts, as indicated by the key. The same line colours are used to show the results for different redshifts in the lower panels. In the upper panel of each plot, we plot two theoretical predictions for the bias parameters, given by Mo et al. (1997) and Scoccimarro et al. (2001).

$\delta_c/\sigma(M, z)$ at different output times are made up of very different numbers of particles]. Gao et al. (2005) were able to measure the linear bias parameter up to haloes corresponding to peak heights of 3σ; we are able to extract measurements for haloes corresponding to 5σ peaks.

In the upper sub-panels of Fig. 7, we show two theoretical predictions for the bias parameters of dark matter haloes. The dotted lines show the predictions from Mo et al. (1997), based on an extension of Press & Schechter's (1974) theory for abundance of dark matter haloes and the spherical collapse model. The solid lines show the calculation from Scoccimarro et al. (2001) which uses the mass function of Sheth & Tormen (1999). Our results tend to best agree with the latter, although the measurements favour a steeper dependence of bias on peak height at all orders. For less rare peaks, neither theoretical model gives a particularly good fit to the simulation results. A similar trend, albeit with more scatter between the results at different output redshifts, was found by Gao et al. (2005) (see also Wechsler et al. 2006; Jing et al. 2007).

Previous studies have reported a dependence of clustering strength on a second halo property besides mass, such as halo formation time or concentration (Wechsler et al. 2006; Gao & White 2007). We do not have sufficient output times to make a robust estimate of formation time so we use a proxy for halo concentration instead, V_{max}/V_{200}. We find that the clustering of high peak haloes is sensitive to the fact that whether the halo has a high or low value of V_{max}/V_{200}. The 20 per cent of haloes with the lowest values of V_{max}/V_{200} within a given mass bin (i.e. those with the lowest concentrations) have the largest linear and second-order bias terms. This result agrees with previous estimates of the dependence of the linear bias term on halo concentration (Wechsler et al. 2006).

The peak height dependence of the third- and fourth-order bias terms for haloes split by V_{max}/V_{200} is more complicated. Fig. 7

shows that the third-order bias depends on our concentration proxy in a non-monotonic fashion. The trend for the fourth-order bias is reversed compared with the results for the first- and second-order bias parameters: low-concentration haloes have a negative value of the fourth-order bias. We note that it would not be possible to measure a fourth-order bias at all using halo autocorrelation functions.

One might be concerned that our results could be sensitive to the operation of the group finder. In particular, it is well known that the FoF algorithm can sometimes spuriously link together distinct haloes into a larger halo, through bridges of particles (e.g. Cole & Lacey 1996). We therefore carried out the exercise of relabelling the mass of each halo by the mass of the largest substructure as determined by SUBFIND. In the rare cases in which haloes are incorrectly linked into a larger structure, using instead the SUBFIND mass would result in a significant shift in the mass bin to which the halo is assigned. Moreover, one would expect that low-concentration FoF haloes would be more prone to being broken up in this way. However, we found no change in our results upon following this procedure, demonstrating that the trends we find for the dependence of bias on mass and concentration are robust.

4 SUMMARY AND DISCUSSION

In this paper, we have combined ultra-large volume cosmological simulations with a novel approach to estimating the higher order correlation functions of dilute samples of objects. The large simulation volume allows us to extract bias parameters on large scales, which follow linear perturbation theory more closely, and provides us with large samples of high-mass haloes from which robust clustering measurements can be made. The cross-moment counts-in-cells technique we use to estimate the higher order clustering of dark matter haloes has superior noise performance to traditional autocorrelation functions, allowing us to probe clustering to higher orders. These improvements made it possible to extend previous work on the assembly bias of dark matter haloes in a number of ways. We have been able to extract measurements of halo clustering for objects corresponding to 5σ peaks, almost twice as high as in earlier studies. We have also presented, for the first time, estimates of the higher order bias parameters of haloes, up to fourth order, and using narrow mass bins.

Our results are in qualitative agreement with those in the literature where they overlap. We find that the linear bias factor, b_1, is a strong function of mass, varying by an order of magnitude for peaks ranging in height from $\delta_c/\sigma(M, z) = 1$ to 5. We use the ratio of the maximum of the effective halo rotation speed to the speed at the virial radius, V_{max}/V_{200} as a proxy for halo concentration. High-mass, high-V_{max}/V_{200} haloes are less strongly clustered than the same mass haloes with low values of V_{max}/V_{200}; haloes with $\delta_c/\sigma(M, z) \sim 4$ display second-order clustering that differs by $\approx$25 per cent between the 20 per cent with the lowest values of V_{max}/V_{200} and the 20 per cent of the population with the highest values of this ratio.

It is reassuring that we recover a similar dependence of the linear bias on halo mass when labelling haloes by V_{max}/V_{200} as other authors found using the concentration parameter (Wechsler et al. 2006). This trend is the opposite to that recovered when halo samples are split by formation time. Gao et al. (2005) found no dependence of the clustering signal on halo formation time for massive haloes. This is puzzling since formation time and concentration are correlated, albeit with scatter (e.g. Neto et al. 2007). Croton et al. (2007) have argued that this suggests that an as yet unknown halo property is a more fundamental property in terms of determining the clustering strength (for theoretical explanations of the physical basis of assembly bias see e.g. Ariel Keselman & Nusser 2007; Zentner 2007; Dalal et al. 2008).

The second-order bias parameter, b_2, displays qualitatively similar dependences on mass and V_{max}/V_{200} to b_1 with the difference that b_2 is negative around $\delta_c/\sigma(M, z) \sim 1$. The third- and fourth-order bias parameters are more complicated, being essentially independent of mass until peaks $\delta_c/\sigma(M, z) \sim$ 2–3 are reached, where there is a dip in bias before a rapid increase for rarer peaks. The dependence on V_{max}/V_{200} is also different at third and fourth order.

We compared our measurements for the bias parameters with analytic predictions. For haloes corresponding to rare peaks, the trend in linear bias versus peak height is intermediate between the predictions of Mo et al. (1997), which are based on Press & Schechter's (1974) theory for the abundance of haloes and the spherical collapse model, and the calculation of Sheth et al. (2001) and Scoccimarro et al. (2001), based on ellipsoidal collapse and an improved estimate of the halo mass function. Both analytic calculations predict a weaker dependence of b_1 on peak height around $\delta_c/\sigma(M, z) \sim 1$ than we find in the simulation. The comparison between the simulation measurements and the analytic predictions is similar for b_2. For the third- and fourth-order bias parameters, the simulation results are in good agreement with the analytic predictions for modest peaks. For rare peaks, the bias parameters measured from the simulation are again in between the two analytic predictions.

Observations of clustering are already entering the regime in which our simulation can play an important role in interpreting the measurements. Existing observations of high-redshift quasar clustering suggesting that these objects live in haloes corresponding to $\sim$5–6 sigma peaks in the matter distribution at $z = 4$ (White, Martini & Cohn 2007). Future galaxy surveys, due to the volume covered and number of galaxies targeted, will yield measurements of clustering with unprecedented accuracy, to higher orders than the two-point function. The measurements presented in this paper will provide invaluable input to future models of galaxy clustering based on halo occupation distribution models, which have been modified such that galaxy clustering is a function of mass and a second halo property.

ACKNOWLEDGMENTS

We acknowledge Liang Gao, Shaun Cole and Carlos Frenk for helpful discussions and Lydia Heck for managing the Cosmology Machine at Durham which was used to run the simulations used in this paper. We also thank Robert Smith, Martin White and Andrew Zentner for useful comments on the preprint version of this paper. REA is supported by a PPARC/British Petroleum sponsored Dorothy Hodgkin postgraduate award. CMB is funded by a Royal Society University Research Fellowship. This work was supported in part by a rolling grant from STFC.

REFERENCES

Angulo R., Baugh C. M., Frenk C. S., Lacey C. G., 2008, MNRAS, 383, 755
Ariel Keselman J., Nusser A., 2007, MNRAS, 382, 1853
Baugh C. M., Gaztanaga E., Efstathiou G., 1995, MNRAS, 274, 1049
Baugh C. M. et al., 2004, MNRAS, 351, L44
Bernardeau F., 1994, ApJ, 433, 1
Bernardeau F., Colombi S., Gaztañaga E., Scoccimarro R., 2002, Phys. Rep., 367, 1

Bett P., Eke V., Frenk C. S., Jenkins A., Helly J., Navarro J., 2007, MNRAS, 376, 215
Cole S., Kaiser N., 1989, MNRAS, 237, 1127
Cole S., Lacey C., 1996, MNRAS, 281, 716
Croton D. J., Gao L., White S. D. M., 2007, MNRAS, 374, 1303
Croton D. J. et al., 2004, MNRAS, 352, 1232
Dalal N., White M., Bond J. R., Shirokov A., 2008, preprint (arXiv:0803.3453)
Davis M., Efstathiou G., Frenk C. S., White S. D. M., 1985, ApJ, 292, 371
Espino-Briones N., Plionis M., Ragone-Figueroa C., 2007, ApJ, 666, 5
Frith W. J., Outram P. J., Shanks T., 2006, MNRAS, 373, 759
Fry J. N., Gaztanaga E., 1993, ApJ, 413, 447
Gao L., White S. D. M., 2007, MNRAS, 377, L5
Gao L., Springel V., White S. D. M., 2005, MNRAS, 363, L66
Gaztanaga E., Baugh C. M., 1995, MNRAS, 273, L1
Ghigna S., Moore B., Governato F., Lake G., Quinn T., Stadel J., 1998, MNRAS, 300, 146
Harker G., Cole S., Helly J., Frenk C., Jenkins A., 2006, MNRAS, 367, 1039
Hoyle F., Szapudi I., Baugh C. M., 2000, MNRAS, 317, L51
Jing Y. P., Suto Y., Mo H. J., 2007, ApJ, 657, 664
Juszkiewicz R., Bouchet F. R., Colombi S., 1993, ApJ, 412, L9
Kaiser N., 1984, ApJ, 284, L9
Lemson G., Kauffmann G., 1999, MNRAS, 302, 111
Lewis A., Challinor A., Lasenby A., 2000, ApJ, 538, 473
Mo H. J., White S. D. M., 1996, MNRAS, 282, 347
Mo H. J., Jing Y. P., White S. D. M., 1997, MNRAS, 284, 189
Navarro J. F., Frenk C. S., White S. D. M., 1997, ApJ, 490, 493
Neto A. F. et al., 2007, MNRAS, 381, 1450
Nichol R. C. et al., 2006, MNRAS, 368, 1507
Peebles P. J. E., 1980, The Large-Scale Structure of the Universe. Research Supported by the National Science Foundation. Princeton Univ. Press, Princeton, NJ, p. 435
Percival W. J., Scott D., Peacock J. A., Dunlop J. S., 2003, MNRAS, 338, L31
Press W. H., Schechter P., 1974, ApJ, 187, 425
Sánchez A. G., Baugh C. M., Percival W. J., Peacock J. A., Padilla N. D., Cole S., Frenk C. S., Norberg P., 2006, MNRAS, 366, 189
Sheth R. K., Tormen G., 1999, MNRAS, 308, 119
Sheth R. K., Tormen G., 2004, MNRAS, 350, 1385
Sheth R. K., Mo H. J., Tormen G., 2001, MNRAS, 323, 1
Scoccimarro R., Sheth R. K., Hui L., Jain B., 2001, ApJ, 546, 20
Smith R. E., Scoccimarro R., Sheth R. K., 2007, Phys. Rev. D, 75, 063512
Springel V., 2005, MNRAS, 364, 1105
Springel V., White S. D. M., Tormen G., Kauffmann G., 2001, MNRAS, 328, 726
Wechsler R. H., Zentner A. R., Bullock J. S., Kravtsov A. V., Allgood B., 2006, ApJ, 652, 71
Wetzel A. R., Cohn J. D., White M., Holz D. E., Warren M. S., 2007, ApJ, 656, 139
White S. D. M., 1994, preprint (astro-ph/9410043)
White M., Martini P., Cohn J. D., 2007, preprint (arXiv:0711.4109)
Zel'Dovich Y. B., 1970, A&A, 5, 84
Zentner A. R., 2007, Int. J. Mod. Phys. D., 16, 763
Zhao D. H., Mo H. J., Jing Y. P., Börner G., 2003, MNRAS, 339, 12

This paper has been typeset from a TEX/LATEX file prepared by the author.